Dynamics of Insect-Inspired Flapping-Wing MAVs: Multibody Modeling and Flight Control Simulations

Hosein Mahjoubi, and Katie Byl

***Abstract*—Research on bio-inspired flapping-wing micro-aerial vehicles (MAVs) has experienced a steady growth over the past two decades. In particular, experiments on insect flight dynamics may provide new solutions for various challenges ranging from morphological design to force control mechanisms. A significant amount of research in this area is focused on modeling and simulation of such dynamics; however, mass of the wings and corresponding inertia effects are often ignored for simplification purposes. In this paper, the MAV is considered to be a structure with three rigid bodies, i.e., a main body and two wings. Wing strokes are limited within the body's transverse plane, though each wing can also passively pitch around its lateral axis. Using the Lagrangian, a dynamic multibody model of this system is developed to «1» analyze the significance of wing mass in flight dynamics and «2» simulate flight control experiments. The employed control approach is based on investigated relationships between mechanical impedance properties of the wing pitch joints and average values of aerodynamic forces. The results suggest that the wings' mass and mechanical impedance properties of the joints can be optimized together to enhance lift/thrust production. In addition, simulations of various flight maneuvers with the optimized model and proposed control approach always demonstrate an agile and stable behavior.**

Keywords*—Insect Flight; Multibody Systems; Micro-Aerial Vehicles; Simulations; Flapping-Wing; Tunable Impedance; Passive Dynamics; Maneuverability.

I. Introduction

In recent years, a considerable amount of work has been concentrated on the study and design of micro-aerial vehicles (MAVs). The main motivation for development of research on this new class of vehicles is the emergence of numerous civilian and military applications that usually have specific requirements in terms of size and mobility. Such applications may vary from surveillance missions to inspection of environments that are either hazardous or difficult to access. Carrying out such tasks – both in indoor and outdoor environments – often calls for exceptional flight capabilities. In addition to high maneuverability and obstacle avoidance, these vehicles must be able to move effectively in reduced spaces, navigate at both high and low velocities and quickly switch between efficient forward/backward and hovering flight. These combined features are well beyond the capabilities of conventional fixed and rotary wing mechanisms. Thus, in search for alternative solutions, many researchers have looked to nature and its flapping-wing mechanisms. Years of evolution have equipped birds and insects with amazing flight capabilities [1-2]. For example, hummingbirds are not only highly agile but also efficient enough to migrate [1].

At present, several prototypes exist that are capable of basic flight maneuvers over short periods of time, e.g., *Harvard's Robotic Fly* [3], *Delfly* [4] and the *Entomopter* [5]. However, there are still many challenges that must be overcome, including hardware miniaturization, power storage, light construction materials, morphological design, and better understanding of the unsteady aerodynamics at low Reynolds numbers.

Research on flapping flight has expanded greatly in recent years. In particular, much work has focused on the aerodynamics involved [6-9]. In these works, flapping-wing dynamics are generally investigated by using standard aircraft equations with six degrees of freedom [10]. However, this approach ignores the mass of the wings and the corresponding inertial effects under the assumption of small relative wing mass with respect to the rest of the body. Few researchers have investigated multibody dynamics and the significance of wing mass in flapping-wing flight [11-12]. A study of the influence of wing mass on dynamics of an ornithopter has been carried out in [12]. There, it has been shown that when masses of the wings are much smaller than body mass, numerical results approach the estimations given by the standard aircraft model. However, a complete dynamic model at small scales remains an open challenge due to nonlinear/unsteady aerodynamics, variable mass distributions, and highly nonlinear motions that characterize the flight of insects and small birds.

In this paper, we model a hummingbird-scale flapping-wing MAV as three rigid bodies; one for the central body and one for each wing. It is assumed that wing stroke motions are actively driven, but that each wing is also able to passively pitch around its lateral axis due to the balance between aerodynamic torque and mechanical impedance of the wing-body connection [13-14]. Using the Lagrangian approach, a multibody dynamic model is derived for this structure that, together with a quasi-steady-state aerodynamic model [10, 15], is employed to investigate the influence of wing masses and their inertial effects on flight dynamics. Our analysis shows that each wing mass and its distribution can be optimized to enhance lift/thrust production.

We then use the optimized model to simulate and control

Both authors are with the Robotics Laboratory, Department of Electrical and Computer Engineering, University of California at Santa Barbara, Santa Barbara, CA 93106, USA (e-mail address: h.mahjoubi@ece.ucsb.edu, katiebyl@ece.ucsb.edu).

This work is funded in part by the Hellman Family Foundation.

motion along basic flight trajectories. The employed control approach is based on a *Tunable Impedance* (TI) method which relies on the observed relationships between mechanical impedance parameters of the wing-body connection and average lift/thrust production [15]. This method has previously provided outstanding results with the standard aircraft model [14-16], and the present work investigates the importance of considering a more accurate multibody dynamic model.

The remainder of this paper is organized as follows. Geometric properties of the body and a brief summary of the aerodynamic model are presented in Sections II and III, respectively. An overview of the multibody dynamic model is given in Section IV. Section V analyzes the overall model for possibility of aerodynamic force optimization. Section VI describes the employed control architecture. The results of simulated flight experiments are presented in Section VII, and Section VIII concludes this work.

II. Geometry of the Flapping-Wing MAV

The free-body diagram of a typical two-winged flapping-wing MAV is illustrated in Fig. 1. This diagram is based on MAVs such as *Harvard's Robotic Fly* [3] whose main body is normally in an upright alignment, i.e., similar to a hummingbird. There are three rigid bodies present: one for the main body and one for each wing. The shape and related parameters of the left wing are shown in Fig. 2. Note that the right wing is the exact mirror of the left wing.

In Fig. 1.b, the stroke angles of both wings are shown by ϕ_1 and ϕ_2. Stroke motion is restricted within $\bar{X}\bar{Y}$ plane, i.e., the transverse plane of the main body. However, each wing is also able to freely rotate around its lateral axis – highlighted by dashed lines in Fig. 1 and represented by $\bar{y}_1$ in Fig. 2. It is assumed that the overall aerodynamic force of each wing is observed at its center of pressure (CoP) while gravitational force affects each wing at its center of mass (CoM). The locations of both points with respect to wing's

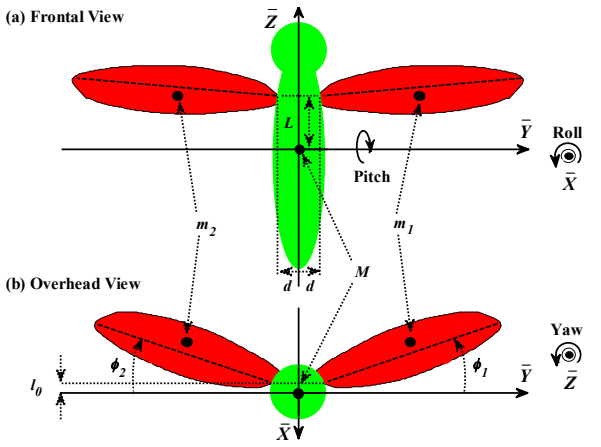

Fig. 1. Free-body diagram of a two-winged flapping-wing MAV: (a) frontal and (b) overhead views. The lateral axis of each wing is highlighted by a dashed line. Position of each wing joint can be located with respect to center of mass of the main body, i.e. *M*, using three parameters: *L*, *d* and l_0. Center of mass of the left and right wings are represented by m_1 and m_2, respectively.

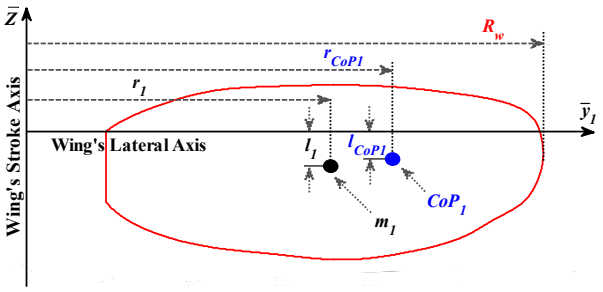

Fig. 2. The shape and related parameters of the left wing. The span of the wing is represented by R_w. *l* and *r* variables are used to define the position of wing's center of mass (m_1) and center of pressure (CoP_1) with respect to wing's lateral and stroke axes.

lateral and stroke axes are shown in Fig. 2. The illustrated geometric parameters are listed in Table I.

III. Aerodynamic Model

We have previously used [10, 18-19] to model the overall aerodynamic force in a hummingbird scale flapping-wing MAV [15]. Here, we only review the final equations for the wing shape in Fig. 2. For further details, see [10,15].

Fig. 3.a shows the normal and tangential components of aerodynamic force at the right wing's center of pressure, i.e., F_N and F_T, respectively. The corresponding lift F_Z and drag F_D components are also illustrated. F_D is composed of two other components: forward and lateral thrusts, i.e., F_X and F_Y as demonstrated in Fig. 3.b.

Using the quasi-steady-state approach described in [15], for each wing with the shape shown in Fig. 2, the aerodynamic forces are estimated as:

$$F_N = -0.0442\rho\,(C_N(\psi)\,\dot{\phi} + 1.3462\ddot{\psi})\,|\dot{\phi}|\,R_W^4 \quad (1)$$

$$F_T = -0.0442\rho\,C_T(\psi)\,\dot{\phi}\,|\dot{\phi}|\,R_W^4 \quad (2)$$

where:

$$C_N(\psi) = 3.4\cos(\psi) \quad (3)$$

$$C_T(\psi) = \begin{cases} 0.4\cos^2(2\psi), & |\psi| \geq \frac{\pi}{4}\ rad \\ 0, & otherwise \end{cases} \quad (4)$$

TABLE I
Geometric Parameters of the Multibody Model

Symbol	Description	Value
R_W	span of each wing in an average hummingbird	8×10^{-2} m
r_i	distance of each wing's CoM from its stroke axis (i = 1,2)	4.632×10^{-2} m
l_i	distance of each wing's CoM from its lateral axis (i = 1,2)	5.645×10^{-3} m
r_{CoPi}	distance of each wing's CoP from its stroke axis (i = 1,2)	5.777×10^{-2} m
l_{CoPi}	distance of each wing's CoP from its lateral axis (i = 1,2)	5.38×10^{-3} m
L	distance of wing joints from CoM of the main body along $\bar{Z}$ axis	2.889×10^{-2} m
d	distance of wing joints from CoM of the main body along $\bar{Y}$ axis	5.777×10^{-3} m
l_0	distance of wing joints from CoM of the main body along $\bar{X}$ axis	5.777×10^{-3} m

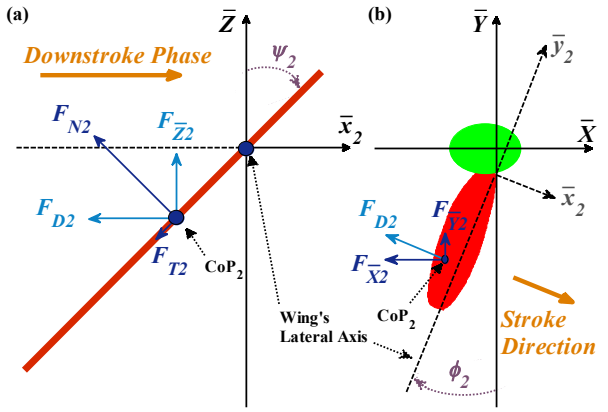

Fig. 3. (a) Right wing's cross-section (during downstroke) at center of pressure, illustrating the pitch angle ψ_2. Normal and tangential aerodynamic forces are represented by F_{N2} and F_{T2}. F_{Z2} and F_{D2} represent the lift and drag components of the overall force. (b) Overhead view of the wing/body setup which demonstrates the stroke angle ϕ_2. F_{X2} and F_{Y2} are components of F_D that represent forward and lateral thrust, respectively.

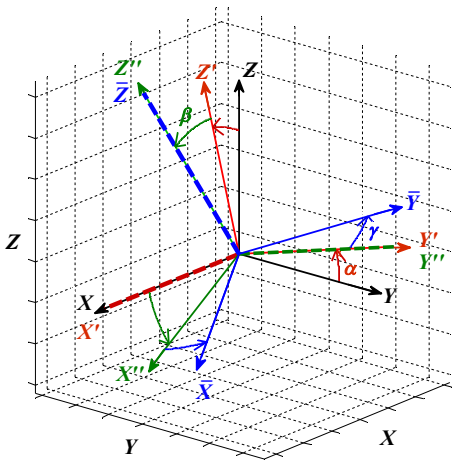

Fig. 4. Transformation from the global reference frame (XYZ) to the local, main body frame ($\bar{X}\bar{Y}\bar{Z}$) involves three consecutive rotations: rotation around X axis by angle α, rotation around Y' axis by angle β and rotation around Z'' axis by angle γ.

are the aerodynamic coefficients [15, 17]. Both coefficients are functions of wing pitch angle ψ, as defined in Fig. 3.a. In (1) and (2), the density of air is shown by ρ while R_W represents the span of the wing (Fig. 2).

From Fig. 3.a, F_Z and F_D can be calculated as:

$$F_{\bar{Z}} = F_N \sin\psi - F_T \cos\psi \tag{5}$$

$$F_D = F_N \cos\psi + F_T \sin\psi \tag{6}$$

F_X and F_Y are also calculated from Fig. 3.b as:

$$F_{\bar{X}} = -F_D \cos\phi \tag{7}$$

$$F_Y = F_D \sin\phi \tag{8}$$

IV. Multibody Dynamic Model

The free-body diagram in Fig. 1 can be used to calculate the location of each body's center of mass along $\bar{X}\bar{Y}\bar{Z}$ axes, i.e., in the local body coordinate system. Choosing the overall center of mass as the origin of $\bar{X}\bar{Y}\bar{Z}$ system, for any set of angles ϕ_1, ϕ_2, ψ_1 and ψ_2 as defined in Fig. 1.b and Fig. 3, the following center of mass coordinates are derived for each of the three bodies:

$$\bar{P}_M = \frac{1}{M_T}\begin{bmatrix} (m_1+m_2)l_0 + m_1A_1 + m_2A_2 \\ (m_2-m_1)d - m_1B_1 + m_2B_2 \\ -(m_1+m_2)L + m_1C_1 + m_2C_2 \end{bmatrix} \tag{9}$$

$$\bar{P}_{m1} = \frac{1}{M_T}\begin{bmatrix} -Ml_0 - (M+m_2)A_1 + m_2A_2 \\ (M+2m_2)d + (M+m_2)B_1 + m_2B_2 \\ ML - (M+m_2)C_1 + m_2C_2 \end{bmatrix} \tag{10}$$

$$\bar{P}_{m2} = \frac{1}{M_T}\begin{bmatrix} -Ml_0 + m_1A_1 - (M+m_1)A_2 \\ -(M+2m_2)d - m_1B_1 - (M+m_1)B_2 \\ ML + m_1C_1 - (M+m_1)C_2 \end{bmatrix} \tag{11}$$

where $M_T = M+m_1+m_2$ is the total mass of the system and:

$$A_i = r_i \sin(\phi_i) + l_i \cos(\phi_i)\sin(\psi_i), \quad i = 1,\ 2 \tag{12}$$

$$B_i = r_i \cos(\phi_i) - l_i \sin(\phi_i)\sin(\psi_i), \quad i = 1,\ 2 \tag{13}$$

$$C_i = l_i \cos(\psi_i), \quad i = 1,\ 2 \tag{14}$$

M, m_1 and m_2 are the masses of the main body and the left /right wings, respectively. The position of each wing's center of pressure, i.e. $\bar{P}_{CoP1}$ and $\bar{P}_{CoP2}$, can be similarly derived in $\bar{X}\bar{Y}\bar{Z}$ coordinate system.

Fig. 4 illustrates how the local $\bar{X}\bar{Y}\bar{Z}$ body frame is related to the global reference frame, XYZ. There are three consecutive rotations involved: rotation around X axis by angle α, rotation around new Y' axis by angle β and finally rotation around new Z'' axis by angle γ. The overall rotation matrix is:

$$R(\alpha,\beta,\gamma) = \begin{bmatrix} c_\beta c_\gamma & s_\alpha s_\beta c_\gamma - c_\alpha s_\gamma & c_\alpha s_\beta c_\gamma + s_\alpha s_\gamma \\ c_\beta s_\gamma & s_\alpha s_\beta s_\gamma + c_\alpha c_\gamma & c_\alpha s_\beta s_\gamma - s_\alpha c_\gamma \\ -s_\beta & s_\alpha c_\beta & c_\alpha c_\beta \end{bmatrix} \tag{15}$$

where c and s are respectively the cosine and sine functions of the indexed angles. Thus, each $\bar{P}$ coordinate set in $\bar{X}\bar{Y}\bar{Z}$ system is mapped to a P coordinate set in XYZ system via:

$$P = R(\alpha,\beta,\gamma)\bar{P} + P_{CoM} \tag{16}$$

Here, $P_{CoM} = [x,\ y,\ z]^T$ represents the position of MAV's overall center of mass in XYZ coordinate system.

Under point mass assumption, the kinetic and potential energies of the model, i.e. T and V, are as follows:

$$T = \frac{1}{2}\left(M\left\|\frac{dP_M}{dt}\right\|^2 + m_1\left\|\frac{dP_{m1}}{dt}\right\|^2 + m_2\left\|\frac{dP_{m2}}{dt}\right\|^2 \right) \tag{17}$$

$$V = M_T g z + K_1(\psi_1 - \psi_{01})^2 + K_2(\psi_2 - \psi_{02})^2 \tag{18}$$

where g is the standard gravity. The last two terms in (18) are the potential energies of mechanical structures that model the wing-body connection. Inspired by muscle-wing connections in insects, in [15] we have shown that each one of these connections can be modeled by a torsional spring:

$$\tau_{\psi i} = K_i(\psi_i - \psi_{0i}), \quad i = 1,\ 2 \tag{19}$$

Here, K_i is the stiffness of the spring while ψ_{0i} represents the

wing's pitch equilibrium angle (as defined in Fig. 4 of [15]). From (19), any deviation from ψ_{0i} due to aerodynamic force F_{Ni} will result in production of a resistive torque $\tau_{\psi i}$.

Using Lagrangian mechanics for the system with kinetic and potential energies described in (17)-(18), the equations of motion can be derived in the following form:

$$\begin{cases} E(q,\dot{q})\ddot{q} = N(q,\dot{q}) + \tau_T \\ q = [\alpha, \beta, \gamma, \phi_1, \phi_2, \psi_1, \psi_2]^T \end{cases} \tag{20}$$

$$\begin{bmatrix} \ddot{x} \\ \ddot{y} \\ \ddot{z} \end{bmatrix} = \frac{1}{M_T} \overline{R} \begin{bmatrix} F_{\bar{X}2} + F_{\bar{X}1} - b_v \dot{\bar{x}}|\dot{\bar{x}}| \\ F_{\bar{Y}2} - F_{\bar{Y}1} - b_v \dot{\bar{y}}|\dot{\bar{y}}| \\ F_{\bar{Z}2} + F_{\bar{Z}1} - b_v \dot{\bar{z}}|\dot{\bar{z}}| \end{bmatrix} - \begin{bmatrix} 0 \\ 0 \\ g \end{bmatrix} \tag{21}$$

Here, b_v is the viscous damping coefficient of the main body. Furthermore:

$$[\dot{\bar{x}}, \dot{\bar{y}}, \dot{\bar{z}}] = [\dot{x}, \dot{y}, \dot{z}]\overline{R} \tag{22}$$

where $[\dot{x}, \dot{y}, \dot{z}]$ represents the velocity of overall center of mass in XYZ coordinate system. The columns of matrix $\overline{R}$ are the projection of $\bar{X}\bar{Y}\bar{Z}$ system's unit vectors in XYZ coordinates. When solving the equations of motion in (20) and (21), $\overline{R}$ is updated at the end of every time step Δt via:

$$\overline{R}_{New} = R(\dot{\alpha}\Delta t, \dot{\beta}\Delta t, \dot{\gamma}\Delta t)\overline{R}_{Old} \tag{23}$$

We assume that at $t = 0$ sec, $\overline{R}$ is equal to the identity matrix $I_{3\times3}$, i.e., $\bar{X}\bar{Y}\bar{Z}$ and XYZ systems are initially aligned.

In (20), the individual entries of matrices E and N are derived using *Mathematica*. Since inertia tensor of the main body is near diagonal [14-15] and its mass is much larger than wings, appropriate modification of entries on the main diagonal of E can approximately take into account the inertial effects of mass distribution in each individual body. The diagonal entries corresponding to α, β, γ, ϕ_1 and ϕ_2 are increased by J_α, J_β, J_γ, $J_{\phi 1}$ and $J_{\phi 2}$, respectively. The diagonal entries corresponding to ψ_1 and ψ_2 are replaced by $J_{\psi 1}$ and $J_{\psi 2}$, respectively. As described in Table II, each J represents a moment of inertia for one of the bodies illustrated in Fig. 1 and Fig. 2. Every entry in vector τ_T is the sum of aerodynamic and gravitational torques that influence the corresponding angular acceleration in vector $\ddot{q}$. In some cases, a linear rotational damping term has been included as well (b_ω and $b_{\psi i}$ in Table II). For the purpose of active stroke control, the entries of τ_T that correspond to ϕ_1 and ϕ_2 also include input torque terms $\tau_{\phi 1}$ and $\tau_{\phi 2}$, respectively.

TABLE II
PHYSICAL PARAMETERS OF THE MULTIBODY MODEL

Symbol	Description	Value
ρ	air density at sea level	1.28 kg·m^{-3}
g	standard gravity at sea level	9.81 m·s^{-2}
M_T	total mass of the modeled MAV	4×10^{-3} kg
m_i	mass of each wing (i = 1,2)	2.5×10^{-4} kg
J_α=J_β	pitch and roll moments of inertia of the main body relative to overall CoM (uniform mass distribution)	4.38×10^{-6} kg·m^2
J_γ	yaw moment of inertia of the main body relative to overall CoM (uniform mass distribution)	1.15×10^{-7} kg·m^2
$J_{\phi i}$	moment of inertial of each wing relative to its stroke axis (uniform mass distribution, i = 1,2)	6.117×10^{-7} kg·m^2
$J_{\psi i}$	moment of inertial of each wing relative to its lateral axis (uniform mass distribution, i = 1,2)	1.955×10^{-8} kg·m^2
b_ω	passive damping coefficient of the main body (pitch, roll and yaw)	3×10^{-3} kg·m^2·s^{-1}
$b_{\psi i}$	passive damping coefficient of each wing (pitch rotation, i = 1,2)	5×10^{-6} kg·m^2·s^{-1}
b_v	viscous damping coefficient of the main body when moving in the air	4×10^{-4} kg·m^{-1}

V. MODEL ANALYSIS AND OPTIMIZATION

Following the work presented in [15], it is assumed that stroke angles of both wings have the same profile:

$$\phi_i = \phi_0 \cos(2\pi f_s t) + \delta, \quad i = 1, 2 \tag{24}$$

where $\phi_0 = \pi/3$ rad is the magnitude of stroke and $f_s = 25$ Hz represents flapping frequency. Both values are chosen based on flapping characteristics of a similarly sized hummingbird [1]. δ is a variable bias that is used to stabilize the main body's pitch angle and will be discussed further in Section VI. Throughout this section, (1)-(8) and (20)-(21) are solved with the following constraints: $\alpha = \beta = \gamma = \delta = 0$ rad, i.e., local and global frames are the same. Hence, the model always maintains its upright orientation.

Using a single-body model, it has been previously observed that mechanical properties of the joint, i.e. K_i and ψ_{0i} ($i = 1, 2$), can be optimized to enhance the average values of aerodynamic forces [14-15]. Here, we will investigate the same possibility with the multibody model, taking into account that each wing's mass and its inertia also affect the production of these forces.

The total mass of the model M_T is assumed to be constant (Table II). To analyze the combined influence of mechanical impedance parameters and masses of the wings, we need to calculate the average lift and forward thrust over one steady stroke cycle. The results for various values of stiffness and wing mass are plotted in Fig. 5.a-b. Similar results for

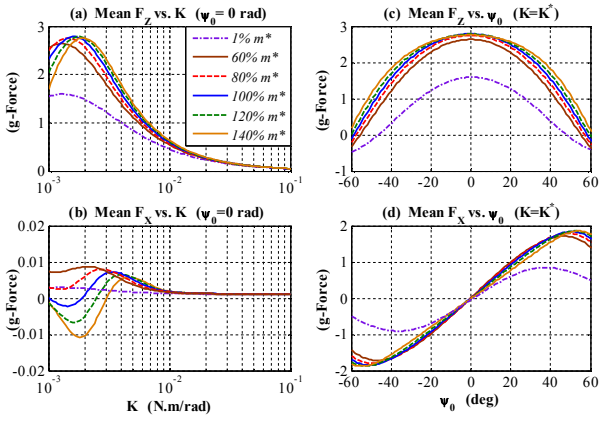

Fig. 5. (a) Average lift and (b) average forward thrust of the MAV vs. stiffness for different values of wing mass. The pitch equilibrium points of both wings are set to 0 rad. (c) Average lift and (d) average forward thrust of the MAV vs. ψ_0 for different values of wing mass. In each case, the stiffness of both wing-joints are set to the corresponding lift-maximizing value in Fig. 5.a, i.e. K^*. $m^* = 2.5\times10^{-4}$ kg is the lift-optimizing value of wing mass. The values of all forces are normalized by the total weight of the model.

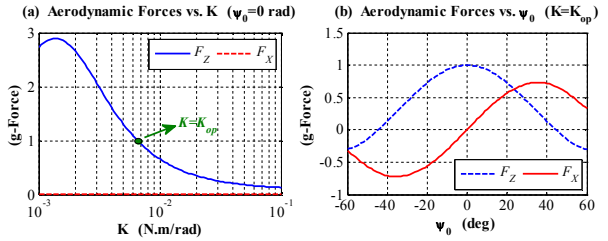

Fig. 6. (a) Average lift and forward thrust of the MAV vs. stiffness. The pitch equilibrium points of both wings are set to 0 rad. (b) Average lift and forward thrust of the MAV vs. ψ_0. The stiffness of both wing-joints are set to $K_{op}=6.7\times10^{-3}$ N·m/rad. In all cases, it is assumed that $m_1=m_2=2.5\times10^{-4}$ kg and $J_{\psi1}=J_{\psi2}=1.0688\times10^{-8}$ kg·m^2. The values of all forces are normalized by the total weight of the model.

various values of $\psi_{01}=\psi_{02}=\psi_0$ and wing mass are illustrated in Fig. 5.c-d. In each case, the moments of inertia of the wings have been recalculated under the assumption of uniform mass distribution. The diagrams in Fig. 5 suggest that under this assumption, $m_1=m_2=m^*=2.5\times10^{-4}$ kg will optimize the force profiles. Note that in one case, the mass of each wing has been reduced to 1% of m^*. The corresponding force diagrams are in agreement with the results of previously investigated single-body model in [15].

Through changes in wing mass distribution, i.e., modifying the values of $J_{\psi1}$ and $J_{\psi2}$, it is possible to further improve the maximum value of average lift. In fact, reducing these values to 54.67% of the original amount – i.e., $J_{\psi i}$ for uniform density in Table II – is the optimum choice. The corresponding diagram for evolution of average lift vs. stiffness is illustrated in Fig. 6.a. From this diagram, when the stiffness of both wing-joints is set to $K_{op}=6.7\times10^{-3}$ N·m/rad, the model generates just enough lift for hovering. Under these circumstances, the evolution of average forward thrust vs. ψ_0 is plotted in Fig. 6.b. Note that for $\psi_0=0$ rad, net production of forward thrust is insignificant. Hence, $K=K_{op}$ and $\psi_0=0$ rad are a suitable choice for nominal values of mechanical impedance parameters during hovering flight.

VI. Flight Control

Fig. 7 illustrates the control structure for each wing. This

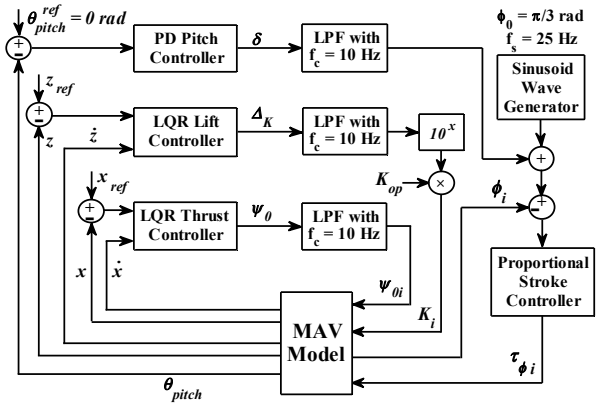

Fig. 7. Block diagram of the proposed *Tunable Impedance* controller for each wing (i = 1, 2) in interaction with MAV model. Cutoff frequency f_c of each low-pass filter is 10 Hz. Both wings employ similar values of δ, K_i and ψ_{0i} at all times. The reference stroke profile properties are always constant: $\phi_0=\pi/3$ rad, $f_s=25$ Hz.

design is based on the *Tunable Impedance* method [14-15] which states that through manipulation of joints' mechanical impedance characteristics around a chosen operation point ($K=K_{op}$ and $\psi_0=0$ rad), it is possible to control the net production of lift and thrust for each wing (Fig. 6) and thus, achieve three-axis control.

Due to constant displacement of each wing's center of pressure with respect to the overall center of mass, the pitch angle of the body θ_{pitch} becomes inherently unstable. To keep this angle small, i.e., to maintain the upright orientation of the model, a PD sub-controller – tuned to $k_p=10$ and $k_d=0.1$ via trial and error – is used to control δ. The output of this controller is limited such that $|\delta|\le\pi/12$ rad. This variable is used to bias the reference stroke profile as described in (24). A proportional controller – with its gain set to 10^3 – regulates input torques $\tau_{\phi1}$ and $\tau_{\phi2}$ such that both wings follow this biased reference stroke profile.

Fig. 6.a suggests that near $K=K_{op}$, average lift is an approximately linear function of $\log_{10}(K)$. In addition, the relationship between average forward thrust and ψ_0 is also close to linear around $\psi_0=0$ rad (Fig. 6.b). Through system identification experiments around this point, i.e., calculation of empirical transfer function estimates followed by *subspace identification method* [19], the corresponding transfer functions were found and used to develop a linear approximation of the dynamics that relate vertical/horizontal positions and velocities to mechanical impedance parameters. The LQR gains of the lift and thrust sub-controllers in Fig. 7 are then calculated for this linearized system:

$$\Delta_K = -20\ (z_{ref}-z)+\dot{z} \tag{25}$$

$$\psi_0 = 75\ (x_{ref}-x)-2.5\dot{x} \tag{26}$$

where x and z are the coordinates of overall center of mass in the XZ plane. Δ_K is a dimensionless parameter while ψ_0 is calculated in radians. The reference flight trajectory within this plane is defined by x_{ref} and z_{ref}. To avoid considerable drift from linear approximation, outputs of these sub-controllers are limited such that $K_i\in[0.2,\ 4]\times10^{-2}$ N·m/rad and $|\psi_{0i}|\le\pi/9$ rad ($i=1,2$).

VII. Simulated Flight Experiments

To investigate the performance of our controller, flight of the optimized MAV model over various trajectories has been simulated. In all cases, the model demonstrates acceptable tracking precision with agile and stable motion. Because of space limitations, here we will only present the results of experiments with three distinct types of trajectories in the XZ plane. With no external disturbance present in these cases, angles α and γ remain equal to 0, resulting in $\beta=\theta_{pitch}$. It is assumed that at $t=0$ sec, the model is hovering at the origin, i.e. $x=z=0$ m. Due to symmetric actuation of both wings, the observed drift along Y axis is always insignificant.

A. Hovering

One of the basic requirements of a practical MAV is the ability to hover. Using the proposed controller in Section VI,

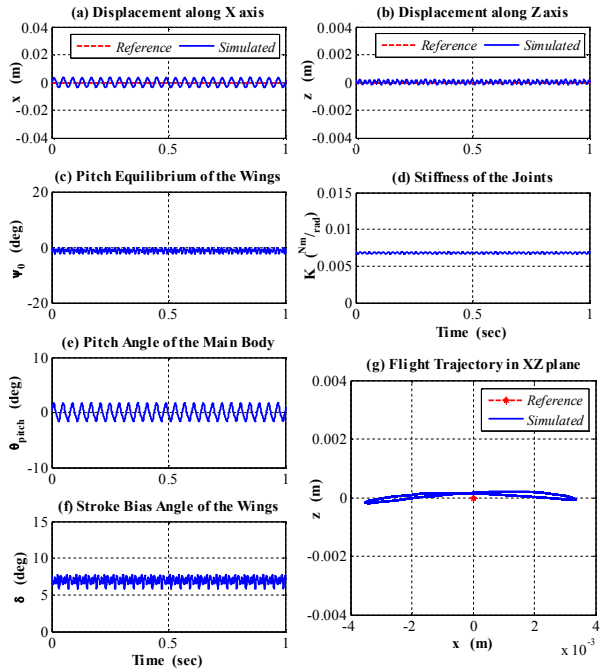

Fig. 8. Hovering at the origin: displacement along (a) X and (b) Z axes, (c) pitch equilibrium angle of the wings ψ_0, (d) stiffness of the joints K, (e) pitch angle of the main body θ_{pitch}, (f) stroke bias angle of the wings δ and (g) flight trajectory in the XZ plane.

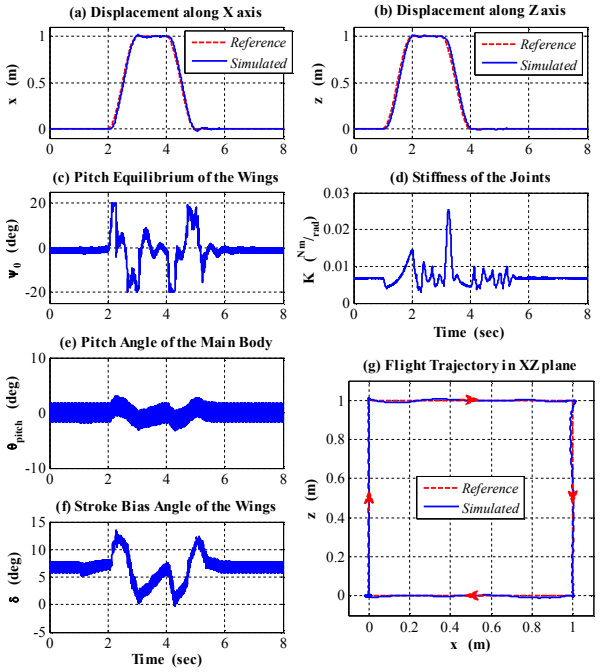

Fig. 9. Flight along a square trajectory: displacement along (a) X and (b) Z axes, (c) pitch equilibrium angle of the wings ψ_0, (d) stiffness of the joints K, (e) pitch angle of the main body θ_{pitch}, (f) stroke bias angle of the wings δ and (g) flight trajectory in the XZ plane.

hovering flight of the multibody model over a period of 1 sec has been simulated. The results are illustrated in Fig. 8. The model always remains close to its original position (Fig. 8.a-b) and maintains its upright orientation (Fig. 8.e). Throughout hovering, outputs of all sub-controllers only experience slight changes (Fig. 8.c-d and f). Fig. 8.g shows the model's overall displacement in the XZ plane. This diagram exhibits a limit cycle behavior which is consistent with observations in [20].

B. Strictly Horizontal/Vertical Motion

Vertical takeoff, descent and forward/backward motion are common modes of flight in various applications of MAVs. Ideally, during such maneuvers the vehicle should only move along one axis. Tracking the square trajectory in Fig. 9.g incorporates every one of these motions. As it is illustrated in Fig. 9.a-b, the controller successfully handles such maneuvers and keeps the model close to reference trajectory. Throughout motion, pitch angle profile of the main body (Fig. 9.e) differs slightly from that of Fig. 8.e; however, it is quickly restabilized upon resumption of hovering mode at $t=5$ sec. Outputs of each sub-controller are also plotted in Fig. 9.c-d and f.

C. Simultaneous Horizontal and Vertical Maneuvers

In trajectories such as the square in Fig. 9.g, motion along one desired axis is handled by either lift or thrust sub-controller. The remaining sub-controller treats any displacement along the other axis as disturbance and attempts to compensate for it. In practice however, most maneuvers require simultaneous motion along both axes. As a result, the performances of aforementioned sub-controllers must not greatly influence each other. To reduce this coupling effect, following the work in [16], we have chosen to use low-pass filters in the control structure (Fig. 7).

As an example of control performance in such scenarios, a diamond-shaped trajectory consisting of ±1 sloped lines has been selected. Tracking of this trajectory requires all possible combinations of simultaneous ascent/descent and

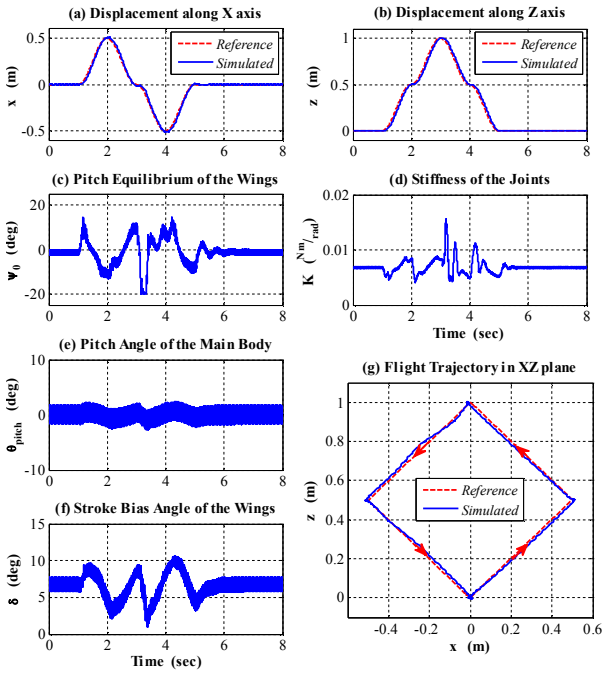

Fig. 10. Flight along a diamond trajectory: displacement along (a) X and (b) Z axes, (c) pitch equilibrium angle of the wings ψ_0, (d) stiffness of the joints K, (e) pitch angle of the main body θ_{pitch}, (f) stroke bias angle of the wings δ and (g) flight trajectory in the XZ plane.

forward/backward motion. The simulated results are illustrated in Fig. 10.a-b and g. Except for a slight drift during backward flight, both x and z coordinates of the model are always close to the reference trajectory. Again, movement may slightly perturb the upright orientation of the model; however, this disturbance is quickly rejected by the pitch sub-controller (Fig. 10.e). Outputs of each sub-controller are also plotted in Fig. 10.c-d and f.

VIII. Conclusion

To investigate the significance of wing mass and inertia in flight dynamics of flapping-wing MAVs, this work develops a multibody model through Lagrangian mechanics. All three considered bodies are modeled as rigid. Furthermore, due to presence of a sub-model for wing-muscle connection, passive wing pitch reversal is possible. Our analysis suggests that models with nonzero wing mass tend to produce larger amounts of net lift and thrust for a given stroke profile (Fig. 5). As wing mass increases, inertial effects enable the wing to reach larger pitch angles before reversing its direction of rotation. This means that for a certain range of wing mass, wing's angle of attack will be close to 45˚ over a significant portion of each flapping cycle. The 45˚ angle of attack is a critical value that, as noted in [17], maximizes the lift coefficient.

Wing mass and inertia can be optimized to enhance aerodynamic force production (Fig. 5 and Fig. 6). To control the optimized model, we have employed a bio-inspired method known as *Tunable Impedance* [15]. Inspired by insect flight, this technique is a semi-passive approach to motion control in flapping-wing MAVs. In short, evolution of each wing's pitch angle ψ_i during a stroke cycle can be manipulated through modification of its joint's mechanical impedance properties. As a result, it is possible to adjust net production of lift and thrust forces (Fig. 6).

The primary advantage of *Tunable Impedance* over conventional force control methods such as *Split Cycle* [21] is its ability to operate without modification of stroke profile. Comparisons between these methods are available in [22-23]. Since magnitude and frequency of stroke remain constant, extra hardware for stroke manipulation in an actual MAV can be replaced by more compact and low-powered impedance manipulators, e.g. [24] or MEMS actuators.

The controller designed on the basis of *Tunable Impedance* demonstrates an agile and stable performance. Furthermore, simulations of various trajectory tracking experiments suggest that motion control through this method can provide reasonable precision. Although the presented trajectories in this work are limited to the *XZ* plane, simulations with a single-body model [25] have shown that with proper modifications, *Tunable Impedance* can also be used to effectively control yaw and roll of the vehicle.

References

[1] D. E. Alexander, *Nature's Flyers*, The Johns Hopkins University Press, 2002.

[2] R. Dudley, *The Biomechanics of Insect Flight: Form, Function, Evolution*. Princeton University Press, 2000.

[3] R. J. Wood, "The first takeoff of a biologically inspired at-scale robotic insect," *IEEE Transactions on Robotics*, 24, pp. 341–347, 2008.

[4] G.C.H.E. de Croon, K.M.E. de Clerq, R. Ruijsink, B. Remes, and C. de Wagter,"Design,aerodynamics,and vision-based control of the DelFly" *International Journal of Micro Air Vehicles*, 1 (2), pp. 71-97, 2009.

[5] R. Michelson, D. Helmick, S. Reece, C. Amarena, "A reciprocating chemical muscle (RCM) for micro air vehicle 'Entomopter' flight," in Proc. of the Association for Unmanned Vehicle Systems International (AUVSI), pp. 429-443, 1997.

[6] C. P. Ellington, "The aerodynamic of hovering insect flight I. the quasi-steady analysis," *Philosophical Transactions of the Royal Society of London*, 305 (1122), pp. 1-15, 1984.

[7] A. Willmott, C. Ellington, C. van den Berg, and A. Thomas, "Flow visualisation and unsteady aerodynamics in the flight of the hawkmoth *Manduca sexta*," *Philosophical Transactions of the Royal Society of London*, *B Biological Sciences*, 352, pp. 303-316, 1997.

[8] S. P. Sane, "The aerodynamics of insect flight," *J. Experimental Biology*, 206, pp. 4191-4208, 2003.

[9] B. Etkin, and L. Reid, *Dynamics of Flight*, Wiley, 1996.

[10] X. Deng, L. Schenato, W. C. Wu, and S. S. Sastry, "Flapping flight for biomimetic robotic insects: part I–system modeling," *IEEE Transactions on Robotics*, 22 (4), pp. 776–788, 2006.

[11] J. Grauer, and J. Hubbard, "Multibody model of an ornithopter," *AIAA J. Guidance, Control, and Dynamics*, 32 (5), pp. 1675-1679, 2009.

[12] C. T. Orlowski, and A. R. Girard, "Modeling and simulation of nonlinear dynamics of flapping wing micro air vehicles," *AIAA Journal*, 49 (5), pp. 969-981, 2011.

[13] H. Mahjoubi, and K. Byl, "Analysis of a tunable impedance method for practical control of insect-inspired flapping-wing MAVs," in Proc. IEEE Conf. on Decision and Control and European Control Conf. (CDC-ECC), pp. 3539-3546, December 12-15, 2011.

[14] H. Mahjoubi, and K. Byl, "Tunable impedance: a semi-passive approach to practical motion control of insect-inspired MAVs," in Proc. IEEE Int. Conf. Robotics and Automation (ICRA), pp. 4621-4628, May 14-18, 2012.

[15] H. Mahjoubi, and K. Byl, "Modeling synchronous muscle function in insect flight: a bio-inspired approach to force control in flapping-wing MAVs," *J. Int. & Robotic Systems*, 70 (1-4), pp. 181-202, 2013.

[16] H. Mahjoubi, and K. Byl, "Trajectory tracking in sagittal plane: decoupled lift/thrust control via tunable impedance approach in flapping-wing MAVs," in Proc. American Control Conf. (ACC), pp. 4951-4956, June 17-19, 2013.

[17] M. H. Dickinson, F. Lehmann, and S. P. Sane, "Wing rotation and the aerodynamic basis of insect flight," *Science*, 284 (5422), pp. 1954-1960, 1999.

[18] Y. Fung, *An Introduction to the Theory of Aeroelasticity*, New York: Dover, 1969.

[19] T. McKelvey, H. Akcay, and L. Ljung, "Subspace-based multivariable system identification from frequency response data," *IEEE Trans. Automatic Control*, 41(7), pp. 960-979, 1996.

[20] D. B. Doman, M. W. Oppenheimer, M. A. Bolender, and D. O. Sigthorsson, "Altitude control of a single degree of freedom flapping wing micro air vehicle," in Proc. AIAA Guidance, Navigation, and Control Conf., August 10-13, 2009.

[21] D. B. Doman, M. W. Oppenheimer, and D. O. Sigthorsson, "Wingbeat shape modulation for flapping-wing micro-air-vehicle control during hover," *J. Guid. Control Dyn.* 33 (3), pp. 724-739, 2010.

[22] H. Mahjoubi, and K. Byl, "Improvement of power efficiency in flapping-wing MAVs through a semi-passive motion control approach," in Proc. Int. Conf. Unmanned Aircraft Systems (ICUAS), pp. 734-743, May 28-31, 2013.

[23] H. Mahjoubi, and K. Byl, "Efficient flight control via mechanical impedance manipulation: energy analyses for hummingbird-inspired MAVs," *J. Int. & Robotic Systems*, 73 (1-4), pp. 487-512, 2014.

[24] J. Choi, S. Hong, W. Lee, S. Kang, and M. Kim, "A robot joint with variable stiffness using leaf springs," *IEEE Transactions on Robotics*, 27 (2), pp. 229-238, April 2011.

[25] H. Mahjoubi, and K. Byl, "Steering and horizontal motion control in insect-inspired flapping-wing MAVs: the tunable impedance approach," in Proc. American Control Conf. (ACC), pp. 901-908, June 27-29, 2012.